Observations and modeling of flexural-mode Lamb waves in box girder bridges using pre-existing telecommunication fiber-optic cables

Jingxiao Liu[a,*], Jatin Aggarwal[b], Doyun Hwang[b], Fu Yin[c], Haipeng Li[d], Hae Young Noh[b,1], Paolo Santi[a,e,1], Carlo Ratti[a,1], Biondo Biondi[d,1]

[a]*Senseable City Laboratory, Massachusetts Institute of Technology, Cambridge, 02139, MA, USA*
[b]*Department of Civil and Environmental Engineering, Stanford University, Stanford, 94305, CA, USA*
[c]*Department of Earth, Environmental, and Planetary Sciences, Rice University, Houston, 77005, TX, USA*
[d]*Department of Geophysics, Stanford University, Stanford, 94305, CA, USA*
[e]*Istituto di Informatica e Telematica del CNR, Pisa, Italy*

Abstract

Bridge superstructures, such as slabs and box girders, behave as plate-like structures where Lamb waves propagate. Lamb wave characteristics are highly sensitive to structural properties and damage. Variations in Lamb wave characteristics can thus serve as indicators of structural changes. However, conventional methods struggle to capture their wavefields due to the high cost of deploying dense sensor networks. This study presents the successful measurement of wavefields of low-frequency (1-70 Hz) flexural-mode Lamb waves in bridge box girders using distributed acoustic sensing (DAS). DAS turns pre-existing telecommunication fiber-optic cables into ultra-dense

*Corresponding author, email: jingxiao@mit.edu
[1]These authors jointly supervised this work.

dynamic-strain-sensing arrays, enabling continuous, high-resolution vibration and seismic monitoring. Through ambient noise interferometry, we reconstruct virtual shot gathers from traffic-induced vibrations, eliminating the need for active seismic sources and minimizing disruptions to regular transportation. This method captures both standing waves (resonance vibrations) and propagating flexural waves, corresponding to the fundamental antisymmetric Lamb wave mode. To validate these observations, we model Lamb wave dispersion by approximating box girders as elastic isotropic plates and Bernoulli-Euler beams, incorporating material properties from design drawings. The strong agreement between modeled and measured dispersion curves confirms the reliability of DAS-recorded flexural waves in box girder bridges. These findings demonstrate the potential of DAS for capturing low-frequency Lamb waves, providing a scalable, real-time solution for bridge condition assessment.
Keywords: Lamb waves, Structural health monitoring, Ambient noise interferometry, Distributed acoustic sensing

1. Introduction

Condition monitoring of bridges is critical for ensuring the long-term safety and resilience of transportation infrastructure [1, 2]. Aging structures, increasing traffic loads, and environmental stressors contribute to progressive deterioration, making early detection of potential damage essential for maintenance and risk mitigation. Conventional sensing methods, such as vi-

bration sensors [3, 4] and vision-based sensors [5, 6], often require costly and labor-intensive deployments of sensor networks, limiting their practicality for large-scale monitoring. To address these limitations, mobile sensing techniques, such as drive-by bridge health monitoring [7, 8], have been introduced to capture high-spatial-resolution information across multiple bridges. However, their transient nature limits temporal resolution at individual locations, restricting their ability to continuously track and diagnose bridge conditions over time [9]. These challenges highlight the need for scalable, cost-effective approaches capable of providing continuous, high-resolution monitoring of bridge conditions.

Recent advancements in distributed acoustic sensing (DAS) have demonstrated its capability to transform pre-existing telecommunication (telecom) optical fiber cables into ultra-dense dynamic-strain-sensing arrays for urban sensing [10, 11]. A DAS system consists of an interrogator unit and a standard optical fiber, where the interrogator injects short laser pulses into the fiber and detects Rayleigh backscattering, which arises from natural inhomogeneities within the fiber [12]. By measuring phase shifts between the outgoing and backscattered signals, the system converts these measurements into strain or strain rate data along the fiber, enabling large-scale, high-resolution sensing. DAS has gained increasing attention in geophysical applications [13, 14, 15] and urban monitoring [10, 16, 17] due to its advantages over conventional single-point sensors. Unlike geophones, Fiber Bragg Gratings, and accelerometers, which provide limited spatial resolution due to

high per-unit costs and logistical constraints, DAS achieves meter-scale spatial resolution over tens of kilometers, effectively creating tens of thousands of sensing channels. This scalability makes DAS a cost-effective solution and a complementary approach for large-scale structural health monitoring.

Liu et al. [18] first demonstrated the use of pre-existing telecom fiber-optic cables as a DAS system for bridge health monitoring, extracting bridge modal parameters such as natural frequencies and mode shapes. Rodet et al. [19] further leveraged this technology to monitor the daily variations in modal parameters across multiple bridges. While these studies provide valuable insights into global bridge dynamics, the potential of DAS for capturing high-resolution wave propagation within bridge superstructures remains largely unexplored.

In this study, we extend DAS-based bridge monitoring by achieving the first successful measurement of low-frequency (1–70 Hz) flexural-mode Lamb waves propagating through box girders using ambient noise interferometry. Bridge superstructures, such as slabs and box girders, behave as plate-like structures where Lamb waves propagate [20, 21]. These waves are sensitive to structural properties, and defects such as cracks or material irregularities cause wave reflection and scattering, making Lamb wave variations valuable indicators of structural damage [22, 23]. However, capturing the wavefields of low-frequency Lamb waves in bridge superstructures has been challenging due to the high cost of deploying dense sensor networks. We address this challenge by leveraging the high spatial resolution of DAS and applying am-

bient noise interferometry to construct virtual shot gathers. This approach enables wavefields reconstruction without active seismic sources, minimizing disruptions to regular transportation.

To evaluate our approach, we conduct field experiments on two box girder bridges with pre-existing telecom fiber-optic cables coupled to their superstructures. Our measurements successfully capture both standing waves (resonance vibrations) and propagating flexural waves, which correspond to the fundamental asymmetric mode of Lamb waves. We further numerically model Lamb wave dispersion curves, approximating the box girders as elastic and isotropic plates using material properties from design drawings. The close agreement between modeled and measured dispersion curves demonstrates the reliability of DAS in capturing low-frequency Lamb waves.

This paper is structured as follows: Section 2 provides background on Lamb waves and their dispersive properties. Section 3 introduces our modeling approach for Lamb waves in box girder bridges. Section 4 details the methodology for constructing Lamb wave virtual shot gathers using ambient noise interferometry. Section 5 describes the DAS dataset used for evaluation. Section 6 presents our results. Sections 7 and 8 discuss potential applications, future directions, and conclusions of this study.

2. Lamb wave modes and dispersion curves

Lamb waves [24] are guided, dispersive waves that propagate in elastic, isotropic plates with free upper and lower surfaces. They arise from the inter-

ference of multiple reflections and mode conversions of body waves (pressure and shear waves) and surface waves (Rayleigh waves) at these free surfaces. For a thin plate of thickness $2d$, as illustrated in Figure 1 (a), the propagation of Lamb waves follows the dispersion equation [25]:

$$\frac{\tan\left(\beta d\right)}{\tan\left(\alpha d\right)} = -\Big[\frac{4\alpha\beta k^2}{(k^2-\beta^2)^2}\Big]^{\pm 1}, \tag{1}$$

where $\alpha^2 = \frac{\omega^2}{V_P^2} - k^2$ and $\beta^2 = \frac{\omega^2}{V_S^2} - k^2$. Here, k is the wavenumber, and V_P and V_S denote the pressure and shear wave velocities, respectively. The $\pm$ sign in Equation (1) distinguishes between symmetric $(+)$ and antisymmetric $(-)$ wave modes relative to the midplane of the plate. The propagation velocities of body waves depend on the material's elastic properties and mass density:

$$V_P = \sqrt{\frac{E(1-\mu)}{\rho(1+\mu)(1-2\mu)}}, \tag{2}$$

$$V_S = \sqrt{\frac{E(1-\mu)}{2\rho(1+\mu)}}, \tag{3}$$

where E, ρ, and μ denote Young's modulus, density, and Poisson's ratio, respectively.

By solving for wave velocities across a broad frequency range [26], dispersion curves for both symmetric (S) and antisymmetric (A) Lamb waves can be obtained. Figures 1 (b) and (c) illustrate the mode shapes of the fun-

damental symmetric (S0) and antisymmetric (A0) Lamb wave modes. The dispersion curves in Figure 1 (d) correspond to a concrete slab with elastic properties representative of normal-strength concrete. The slab has a Young's modulus of 25 GPa, a Poisson's ratio of 0.17, a density of 2400 kg/m^3, and a total thickness of 1 m (d=0.5 m). The fundamental modes are particularly significant as they exist across the entire frequency spectrum, originating at zero frequency. At low frequencies, where the wavelength exceeds the plate thickness, these modes are commonly referred to as the extensional mode (symmetric) and flexural mode (antisymmetric), reflecting their distinct motion characteristics and the elastic stiffness governing their velocities. As frequency increases, higher-order wave modes emerge, each appearing at a specific cutoff frequency and existing only above that threshold. By matching theoretical Lamb wave dispersion curves with experimental data, key material properties, wave velocities, and plate thickness can be estimated. This capability makes Lamb waves widely applicable in non-destructive evaluation for material characterization and thickness measurements of elastic plates [25, 27].

3. Modeling Lamb waves in box girder bridges

Lamb waves propagate through bridge structures and their individual plate-like components. In ultrasonic testing [28, 29], transducers generate Lamb waves in plate-like structural elements, such as slabs, webs, and flanges of girders and beams. By analyzing changes in wave propagation, these

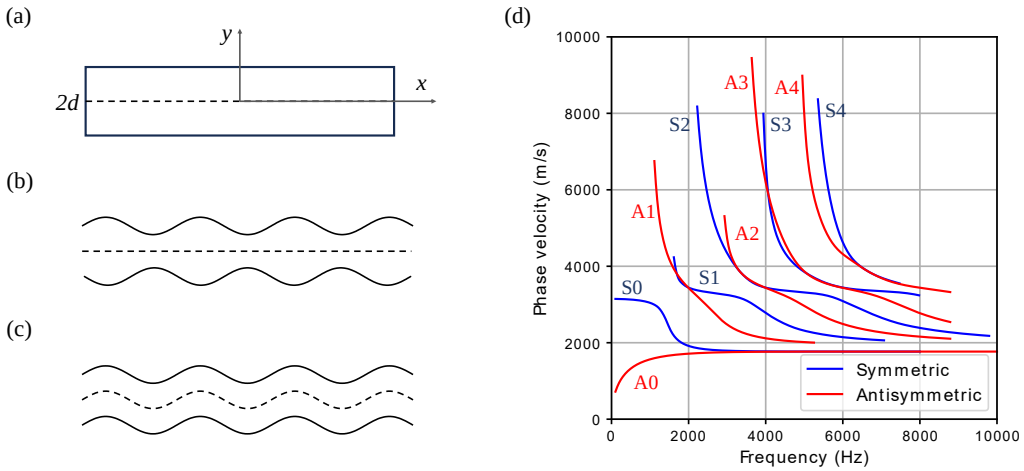

Figure 1: Lamb wave modes and dispersion curves. (a) A thin plate of thickness $2d$. (b) and (c) Mode shapes of the fundamental symmetric and antisymmetric Lamb wave modes, respectively. (d) Top 5-mode dispersion curves for a concrete slab with elastic properties representative of normal-strength concrete. The slab has a Young's modulus of 25 GPa, a Poisson's ratio of 0.17, a density of 2400 kg/m^3, and a total thickness of 1 m (d=0.5 m).

techniques detect cracks, delamination, and other localized structural defects. At lower frequencies (e.g., below 100 Hz), where the wavelength exceeds the thickness of the box girder, the entire box girder behaves as a hollowed plate, as shown in Figure 2 (a). In this regime, Lamb waves propagate through the entire box girder rather than being confined to individual components. This characteristic enables their use for global bridge assessment, capturing structural responses over long distances, and identifying large-scale structural changes and damage.

To examine Lamb wave propagation across the entire box girder, we approximate the hollow box girder as a Bernoulli-Euler (thin) beam with a uniform rectangular cross-section. Figure 2 (b) illustrates a typical box girder

cross-section, while Figure 2 (c) presents the cross-section of the simplified beam model, assumed to behave as a thin plate. The effective Young's modulus, E, is estimated using the fundamental mode resonant frequency:

$$E = \frac{(2\pi f_0)^2 m L^4}{a^4 I}, \tag{4}$$

where f_0, m, L, and I represent the fundamental mode resonance frequency, mass per unit length, span length, and moment of inertia of the box girder, respectively. The parameter a is a constant determined by both the cross-section and boundary conditions. Three types of boundary conditions for a uniform cross-section are considered, as shown in Table 3. The detailed derivation of a can be found in [30]. The effective density, ρ, is given by:

$$\rho = \frac{m}{2wd}, \tag{5}$$

where w is the width and d is half the depth of the box girder.

Table 1: Values of a for different boundary conditions.

Boundary	**Hinged and hinged**	**Fixed and hinged**	**Fixed and fixed**
Schematic	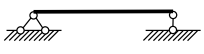	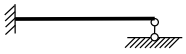	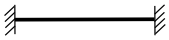
a	π	3.927	4.739

Resonance is a fundamental property of structural dynamics in plates, occurring when left- and right-propagating waves superpose at finite speeds to form standing waves [31, 32]. At resonance, constructive interference amplifies vibration amplitudes, producing standing waves that oscillate in place

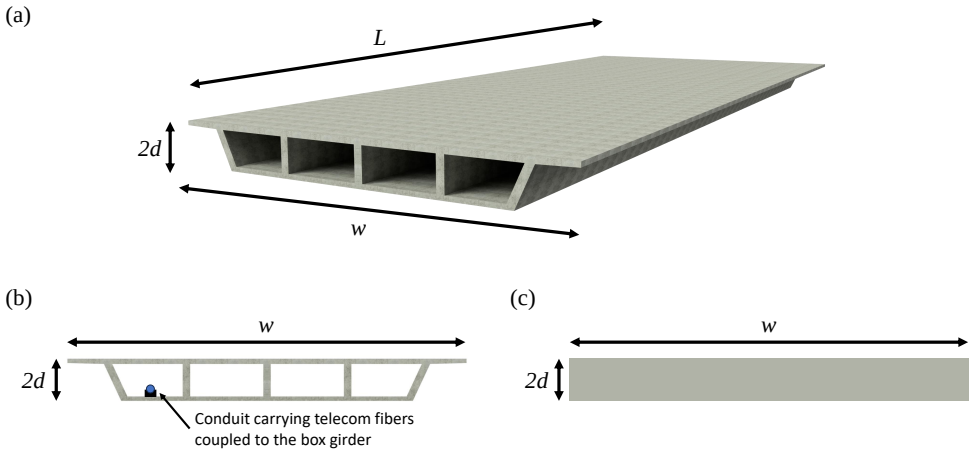

Figure 2: The box girder as a plate. (a) and (b) show a three-dimensional view and cross-section of a box girder. (c) illustrates the cross-section of the simplified beam model, where the box girder is approximated as a thin plate. (b) also shows the conduit carrying telecom fibers coupled to the box girder, representing the setup of tested Bridge 2 in this study, with details provided in Section 5.

rather than propagating through the structure. These waves reflect off structural boundaries and interact with incoming waves, creating interference patterns that define the system's dynamic response. As frequency increases and wavelengths shorten, the system reaches specific resonant frequencies where wave interactions lead to either destructive interference (anti-resonance), causing amplitude cancellation, or constructive interference (resonance), reinforcing wave amplitudes. The resonance conditions for a simplified bridge structure, modeled as a Bernoulli-Euler (thin) beam, are determined by the relationship between the bridge's span length and the wavelength of propagating waves. Resonance occurs when the span length is an integer multiple

of half the wavelength:

$$L = n\frac{\lambda}{2}, \quad n = 1, 2, \ldots \tag{6}$$

where the wavelength is given by $\lambda = v/f$ with n representing the mode number, L the span length, v the wave velocity, and f the wave frequency. This leads to the following relationship between wave velocity and resonance frequency for the fundamental mode:

$$v = 2f_0 L. \tag{7}$$

This modeling framework provides the basis for understanding the propagation of both propagating and standing Lamb waves in box girder bridge superstructures at low frequencies. However, as frequency increases and the wavelength becomes smaller than the girder thickness, material anisotropy and structural complexities become more pronounced, leading to deviations from these simplified assumptions.

4. Constructing Lamb wave virtual shot gathers

Unlike traditional ultrasonic testing, which uses high-frequency transducers to generate Lamb waves, capturing low-frequency flexural-mode Lamb waves (e.g., below 100 Hz) in operational bridges poses significant challenges. Effectively measuring their wavefield changes requires a dense sensing array to track wave propagation accurately. Moreover, generating active seismic

sources, such as vibroseis trucks, on an operational bridge is impractical due to safety concerns and potential traffic disruptions.

To address these limitations, we use DAS to transform pre-existing telecom fiber-optic cables into ultra-dense dynamic-strain-sensing arrays, enabling continuous wavefield recording without additional sensor deployment. Instead of relying on active sources, we harness traffic-induced vibrations as passive seismic sources. To extract coherent wavefields from these ambient vibrations, we construct Virtual Shot Gathers (VSGs), which synthesize wave propagation from a virtual source location. It yields VSGs from the chosen source with other locations as receivers, effectively retrieving the empirical Green's function without using an active source survey.

VSGs are constructed using ambient noise interferometry [33, 34], a technique widely applied in passive seismology to extract coherent wavefields from continuous seismic recordings at different sensor locations. Mathematically, this method is based on the cross-correlation of recorded wavefields. Let $u(x,t)$ represent the recorded DAS dynamic strain data at a sensor location x and time t. The empirical Green's function between two sensor locations x_i and x_j is approximated by the cross-correlation of the wavefields recorded at the two sensors over a time window T:

$$G(x_i, x_j) \simeq \frac{1}{T} \int_0^T u(x_i, t) u(x_j, t+\tau) dt, \tag{8}$$

where τ is the time lag. The empirical Green's function represents an es-

timate of the system's impulse response, characterizing wave propagation between two points, including travel time, dispersion, and structural interactions.

Figure 3 illustrates the cross-correlation process in ambient noise interferometry. The bridge, represented by the rectangular box, is continuously subjected to various noise sources. Traffic-induced vibrations serve as dominant wave sources, generating consistent energy recorded at DAS channels. Other background noise (depicted as stars) introduces scattered ambient vibrations from the surrounding environment. The red triangles mark two DAS channels at x_1 and x_2 along the telecom cable, represented by the black line. The recorded waveforms at x_1 and x_2 contain both traffic-induced vibrations and background noise. To extract meaningful wave propagation characteristics, the signals recorded at these DAS channels are cross-correlated. By stacking (summing) the cross-correlations from multiple noise sources over time, energy from the stationary zone that has traveled along the path between x_1 and x_2 adds constructively, while uncorrelated energy outside the stationary zone is suppressed due to destructive interference. As a result, the retrieved signal approximates the Green's function between x_1 and x_2, as if one of these locations were an active source. This extracted Green's function effectively acts as a seismogram from a virtual source at the location of one of the receivers [35]. Applying this approach to virtual source locations on or near the bridge enables us to reconstruct and analyze propagating waves along the bridge superstructure as captured by DAS.

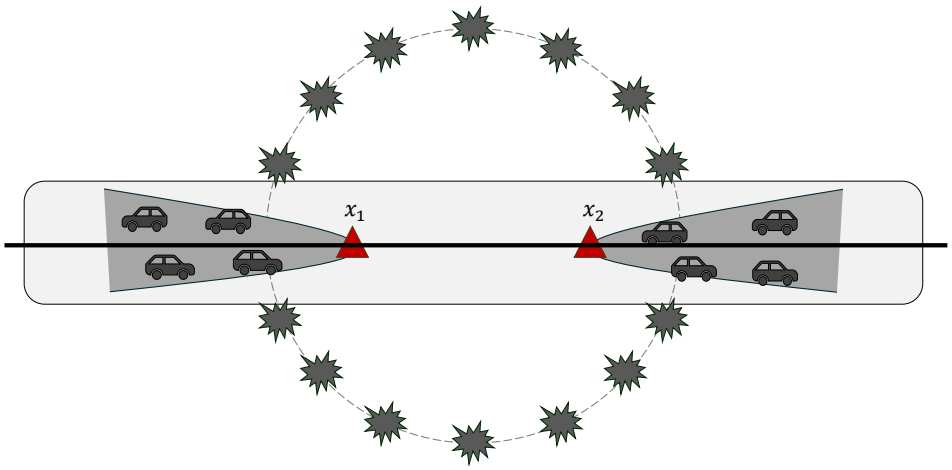

Figure 3: Ambient noise interferometry. The bridge, represented by the rectangular box, is continuously subjected to various noise sources, including traffic-induced vibrations and random background noise (depicted as stars). The triangles mark two DAS channels located at x_1 and x_2 along the telecom cable, represented by the black line. The shaded areas indicate stationary zones, where traffic-generated signals dominate the recorded wavefield.

5. DAS data description and preprocessing

The data for this study were collected in San Jose, California, in September 2023 [10], using a QuantX interrogator from Luna-OptaSense [36] operating at a maximum sampling frequency of 200 Hz. The telecom fiber-optic cables are coupled along the bottom flange of the box girders in both bridges, as illustrated in Figure 2 (b). The two monitored structures, McKee Road over U.S. Highway 101 Overpass (referred to as Bridge 1) and Yerba Buena Road over Coyote Creek (Bridge 2), are prestressed concrete continuous bridges with box girder spans (Figure 4). Both bridges feature monolithic girder-pier connections, where the superstructure and substruc-

ture are rigidly connected without bearings. Bridge 1 consists of two spans measuring 41 meters and 44 meters, with a total length of 84 meters, while Bridge 2 has three spans measuring 29 meters, 39 meters, and 28 meters, totaling 97 meters. Table 2 summarizes key structural properties, including moment of inertia, mass per unit length, and box girder dimensions. Bridge 2's properties were obtained from design drawings, whereas Bridge 1's properties were estimated by assuming a similar box girder cross-section with variations in width and depth, inferred from street-view images due to the absence of design drawings.

Figure 4: Street view images (Google Maps) of (a) Bridge 1, McKee Road over U.S. Highway 101 Overpass and (b) Bridge 2, Yerba Buena Road over Coyote Creek Bridge.

For data collection, the DAS channel spacing for both bridges was set to 1 meter. Bridge 1 was monitored for two days with a gauge length of 2 meters, while Bridge 2 was monitored for six days with a gauge length of 10 meters. In

DAS, gauge length determines the spatial averaging of strain measurements, influencing both resolution and sensitivity. A shorter gauge length offers higher spatial resolution but lower sensitivity, whereas a longer gauge length enhances sensitivity at the cost of resolution. The difference in gauge length was dictated by constraints on data storage capacity and the duration of the collection period. Figure 5 presents one-minute samples of DAS data from both bridges, where vehicle-induced signals appear as distinct trajectories with increased amplitude. The dotted lines indicate bridge joints and piers. To validate DAS measurements, conventional accelerometers were deployed on the bridge decks to record structural vibrations. Figure 6 compares the power spectral density (PSD) obtained from DAS and accelerometer data, showing consistent dominant frequencies across both sensing systems. The fundamental mode resonance frequencies were identified as 2.50 Hz for Bridge 1 and 2.75 Hz for Bridge 2.

Table 2: Bridge properties.

	$I\ (m^4)$	$m\ (kg/m)$	$w\ (m)$	$2d\ (m)$
Bridge 1	3.97	20,712	21	1.70
Bridge 2	3.08	16,464	16	1.70

The DAS data are preprocessed to enhance the signal quality. This process includes removing the mean and linear trend, applying a high-pass filter at 0.01 Hz to eliminate static signals, performing time-domain normalization, and applying spectral whitening at the frequency domain [37] to mitigate the effects of anomalous frequency signals. Next, the seismic data are di-

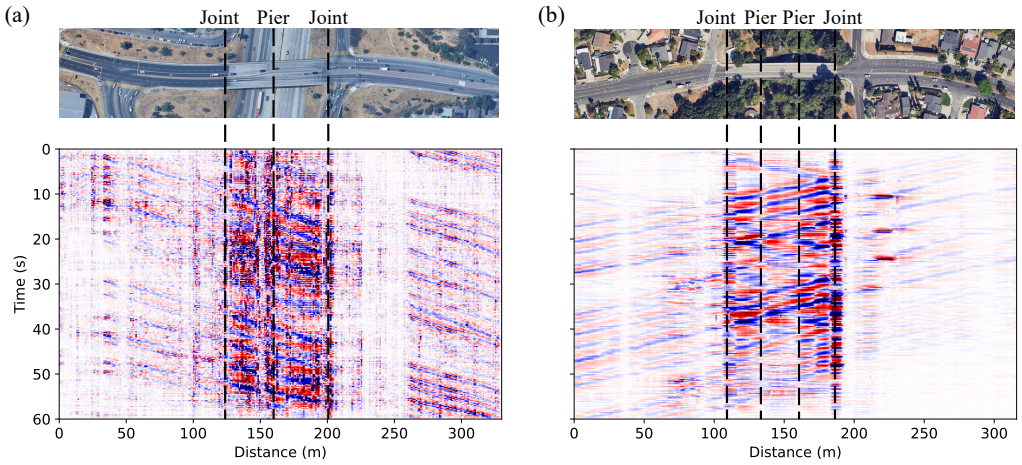

Figure 5: One-minute DAS data for (a) Bridge 1 and (b) Bridge 2. The trajectories observed in the DAS data are quasi-static signals resulting from deformation induced by vehicle loads [13].

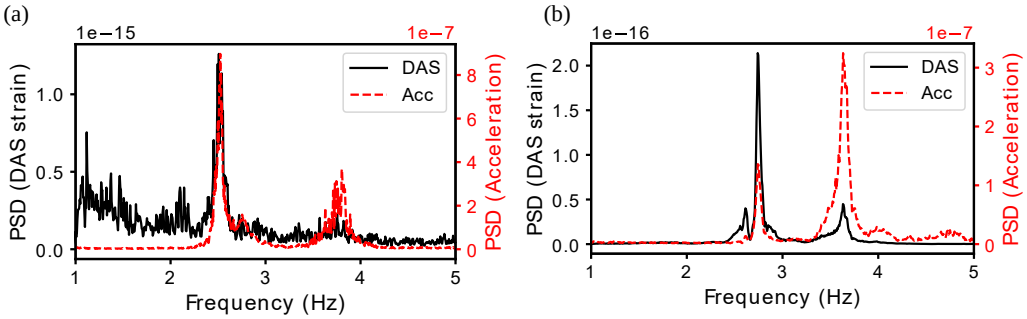

Figure 6: Comparison of Power Spectral Density (PSD) between DAS and accelerometer (Acc) measurements for (a) Bridge 1 and (b) Bridge 2. The color version of this figure is available in the electronic edition only.

vided into one-minute segments for each channel. These segments are then cross-correlated, normalized, and stacked over the entire recording period to produce the final cross-correlation function.

6. Results

This section first examines standing and propagating wave patterns observed in VSGs and then analyzes their dispersion properties by comparing measured phase velocities with theoretical models from Section 3.

6.1. Characterizations of flexural-mode Lamb waves

Distinct propagating and standing flexural-mode Lamb waves are observed in the constructed VSGs. Figure 7 presents the VSG results for both bridges across the full frequency band. The virtual source locations, marked by yellow triangles, are positioned near bridge joints to capture wave propagation across the entire superstructure. The horizontal, phase-aligned signals correspond to standing wave patterns, representing the bridge's resonance vibrations. These standing waves arise from constructive interference of multiple reflections within each span, forming a stationary oscillation pattern. The spatial variation of standing waves exhibits alternating red and blue oscillation patterns corresponding to the number of spans in each bridge. These color variations indicate phase differences in resonance vibrations, with nodal points forming near the bridge piers and joints due to wave interference. In Bridge 1 (Figure 7 a), two standing wave phases emerge, reflecting its two-span structure, while Bridge 2 (Figure 7 b) exhibits three standing wave phases, aligning with its three-span configuration.

Filtering out resonance frequencies enhances the visibility of propagating Lamb waves. Figure 8 presents the VSGs after applying a notch filter (band-

rejection filter) at the natural frequencies to remove resonance signals. We can observe propagating waves propagate at approximately 400 m/s at 12 Hz for Bridge 1 and 350 m/s at 15 Hz for Bridge 2. Wave reflections are also clearly observed at bridge piers and joints, where abrupt structural changes cause partial wave energy to reflect back toward the source. These reflections provide valuable insights into potential structural discontinuities and variations in boundary conditions or material properties. Furthermore, Lamb waves do not propagate beyond the bridge joints leading to the ground ramps, indicating a discontinuity in wave transmission at these structural transitions. This highlights the sensitivity of flexural-mode Lamb waves to boundary conditions and structural connectivity. Additionally, waves observed on the ground surface (before the left joint and after the right joint) exhibit different propagation characteristics, suggesting they are surface waves rather than flexural Lamb waves. These surface waves are likely influenced by soil-structure interactions, subsurface structures, and ground coupling effects.

6.2. Lamb wave dispersion analysis

Lamb waves are dispersive, where phase velocities vary with frequency. To obtain stable dispersion spectra for the flexural-mode Lamb waves in the box girder, we construct VSGs using virtual source locations within 15 meters on either side of bridge joints. Setting virtual sources near the bridge entry ensures that VSGs capture propagating waves across the entire box girder. Dispersion spectra for each VSG location are then derived using the

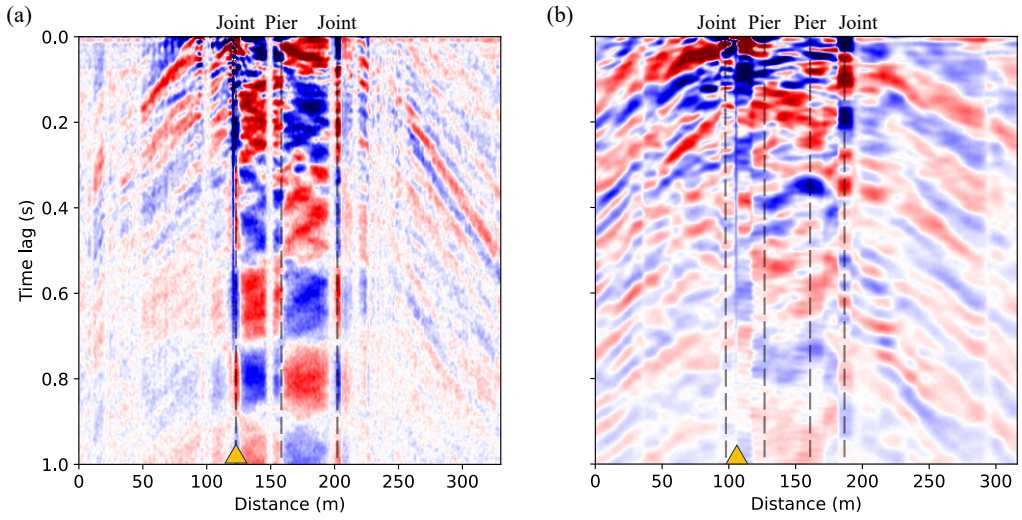

Figure 7: Virtual shot gather results for (a) Bridge 1 and (b) Bridge 2, using signals across the full frequency band. Dotted lines indicate the locations of bridge joints and piers, while yellow triangles mark the virtual shot locations. The color version of this figure is available only in the electronic edition.

phase-shift method [38]. To further improve signal clarity, dispersion spectra from different virtual source locations for each bridge are stacked, effectively reducing random noise. Figure 9 presents the measured dispersion spectra for the two bridges. Panels (a) and (b) show raw spectra, while (c) and (d) display frequency-normalized spectra, highlighting wave energy distributions across frequency bands. The white lines mark the wavelengths corresponding to the gauge length, below which spatial high-cut filtering occurs due to the finite gauge length.

Theoretical dispersion curves for flexural-mode Lamb waves are modeled using the method described in Sections 2 and 3. The box girders are approximated as thin beams with rectangular cross-sections. Since both bridges

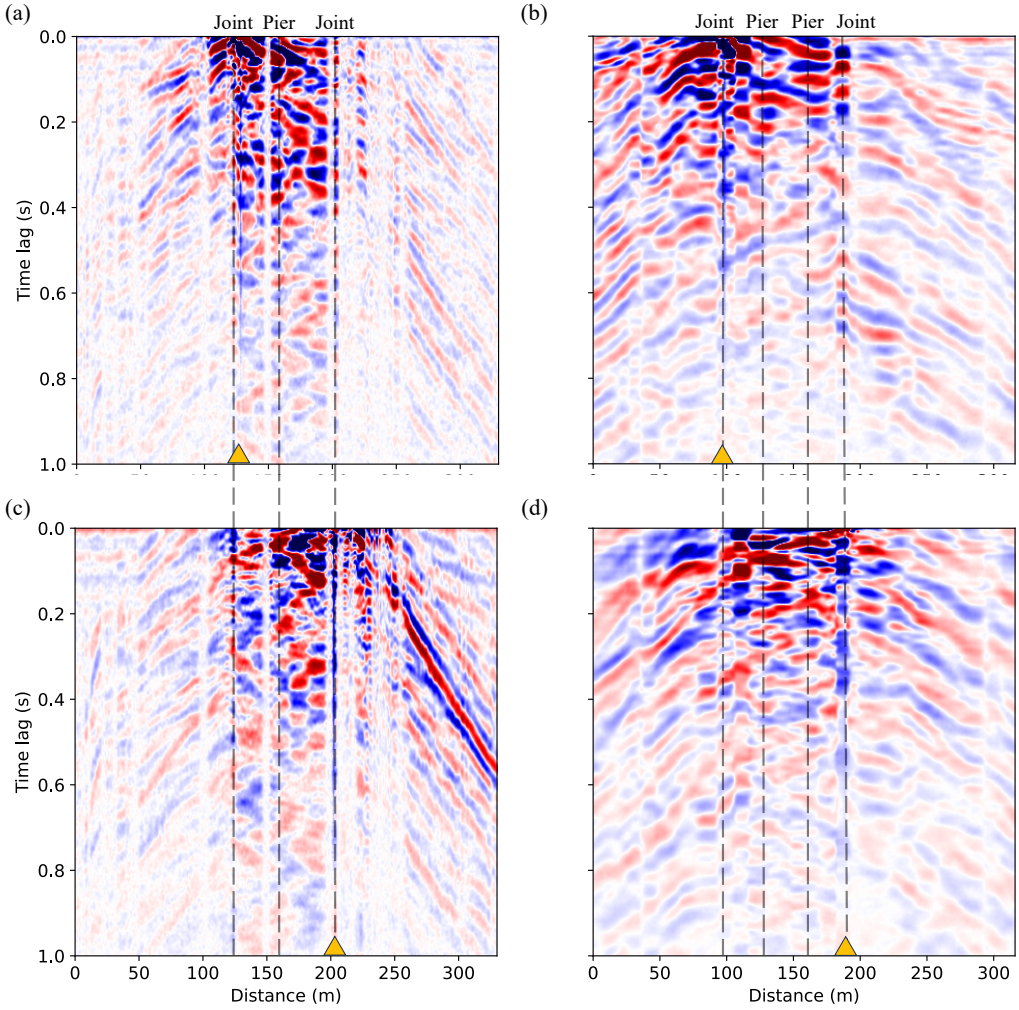

Figure 8: Virtual shot gather results for Bridge 1 (a and c) and Bridge 2 (b and d) after applying a notch filter (band-rejection filter) to remove resonance frequency signals. Dotted lines indicate the locations of bridge joints and piers, while yellow triangles mark the virtual shot locations. The color version of this figure is available only in the electronic edition.

feature monolithic girder-pier connections, appropriate boundary conditions are applied, as illustrated in Figure 10. Bridge 1 is modeled with fixed-hinged boundary conditions for both spans, while Bridge 2 is modeled with a

fixed-fixed condition for the middle span and fixed-hinged conditions for the outer spans. These boundary conditions define the parameter a required for calculating the effective Young's modulus, as listed in Table 3. Structural variations between the two bridges, such as different span lengths, are also incorporated into the model. Material properties of the two bridges – including the range of effective Young's modulus, effective density, and Poisson's ratio – are estimated using Equations (4) and (5), based on the structural parameters listed in Table 2 and the fundamental mode resonance frequencies identified from DAS and accelerometer measurements. The corresponding pressure wave velocity (V_P) and shear wave velocity (V_S) are derived using Equations (2) and (3), with values listed in Table 4. These velocity estimates are used to model the Lamb wave dispersion curves, shown as the shaded region in Figure 9.

Table 3: Estimated effective material properties of the bridges.

	E (Pa)	ρ (kg/m^3)	μ
Bridge 1	$[1.46 \times 10^{10}, 2.01 \times 10^{10}]$	580	0.17
Bridge 2	$[7.15 \times 10^{9}, 4.31 \times 10^{9}]$	605	0.17

Table 4: Estimated wave velocities for the two bridges.

	V_P (m/s)	V_S (m/s)
Bridge 1	[5195, 6104]	[2985, 3507]
Bridge 2	[2765, 3564]	[1589, 2047]

The measured dispersion spectra closely align with the modeled dispersion curves up to approximately 70 Hz for both bridges, demonstrating consistency between observed and theoretical wave behavior. However, at fre-

quencies above 70 Hz, discrepancies emerge, likely due to the limitations of the isotropic and homogeneous assumptions in the modeling. As wavelengths shorten at higher frequencies, the heterogeneous nature of the box girder—including material anisotropy and structural details—becomes more influential, deviating from the simplified theoretical model. Additionally, Bridge 1 exhibits cleaner dispersion spectra compared to Bridge 2, which may be attributed to differences in gauge length. The longer gauge length in Bridge 2 results in lower spatial resolution, leading to increased spectral smearing and reduced precision in capturing fine dispersion features. This highlights the trade-off between gauge length and spatial resolution in DAS-based measurements. In the 1.5–5 Hz frequency band, Figure 9 (e) and (f) show the modeled standing wave velocity derived from Equation (7), overlaid with the estimated frequency for the first span of both bridges. The agreement between modeled and measured wave behavior validates that standing waves arise from the superposition of left- and right-propagating Lamb waves, satisfying the Equation (6). The discrepancy between the measured dispersion spectra and the modeled dispersion mode in the 1–5 Hz frequency range for Bridge 2 may be due to its long gauge length measurements or complex span configuration.

7. Discussion

This study presents the successful measurement of wavefields of low-frequency (1–70 Hz) flexural-mode Lamb waves propagating through box

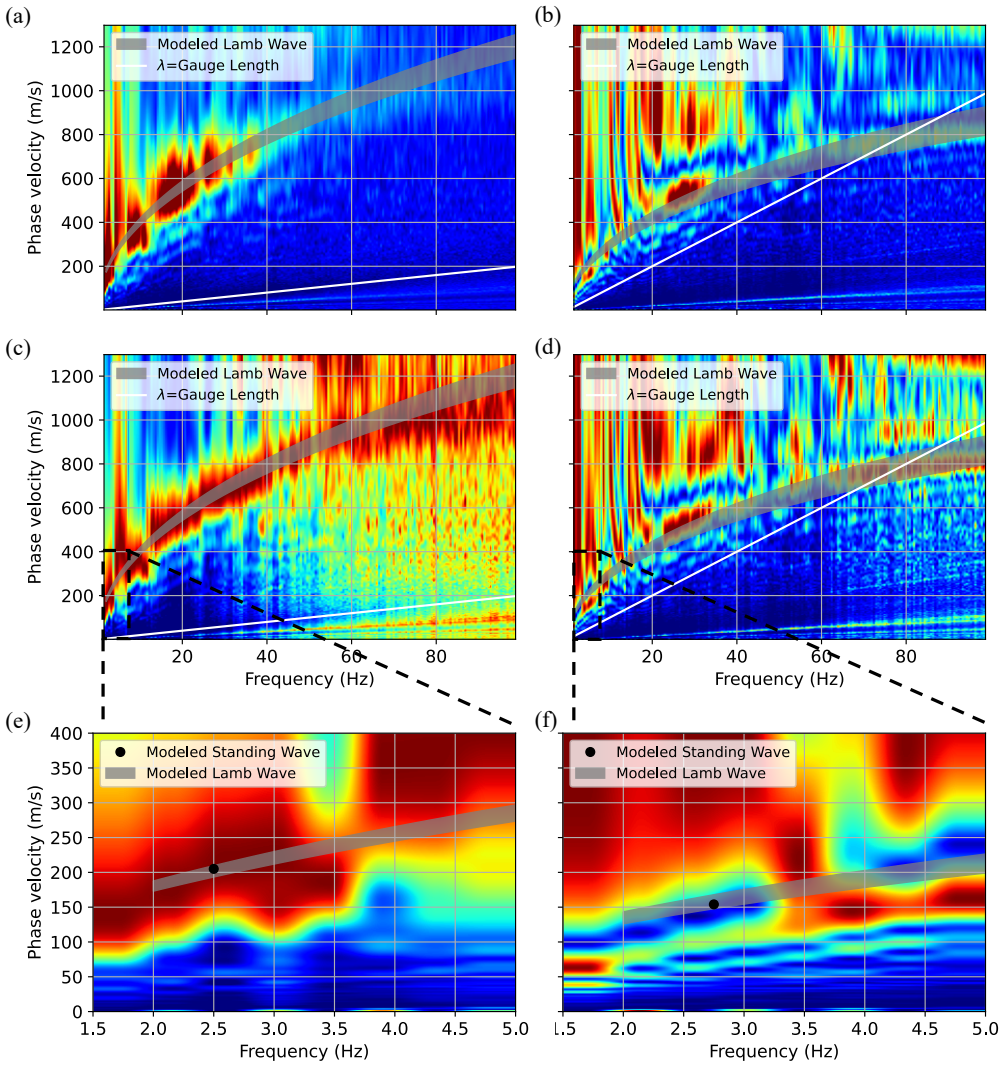

Figure 9: Dispersion measurements for Bridge 1, McKee Road over U.S. Highway 101 Overpass (a,c, and e) and Bridge 2, Yerba Buena Road over Coyote Creek Bridge (b, d, and f). Panels (a) and (b) show the dispersion spectra without normalization, while (c) and (d) present the spectra normalized by frequency. The white lines mark the wavelengths corresponding to the gauge length, below which spatial high-cut filtering occurs due to the finite gauge length. Panels (e) and (f) provide a zoomed-in view of the dispersion spectra, focusing on the 0–400 m/s phase velocity range and 1.5–5 Hz frequency range. The color version of this figure is available only in the electronic edition.

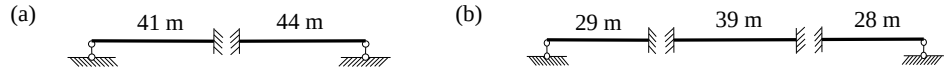

Figure 10: Schematic representations of (a) Bridge 1 and (b) Bridge 2. Numbers indicate the respective span lengths.

girder bridges. By using pre-existing telecom fiber-optic cables as dense sensing arrays with DAS, we achieve high-resolution wavefield measurements. The integration of DAS with ambient noise interferometry enables the extraction of wave propagation characteristics from traffic-induced vibrations, eliminating the need for external excitation.

Despite these promising findings, several limitations merit future works:

- The DAS system used in this study operates at a maximum sampling frequency of 200 Hz, limiting our ability to observe higher-mode Lamb waves. Future research should explore higher-frequency wave propagation using DAS, which could introduce additional constraints for structural property inversion and enable more refined and localized assessments of bridge conditions.

- Our current modeling approach approximates the box girder as an elastic isotropic plate and a Bernoulli-Euler beam. While this simplification is effective at low frequencies—where the wavelength exceeds the girder thickness—it may not hold at higher frequencies, where geometric and material heterogeneity becomes more significant. Future work should incorporate finite element modeling to account for complex wave in-

teractions and structural details, improving the accuracy of simulated wave propagation in bridge superstructures.

- An important next step is to develop inversion techniques for estimating structural properties from measured dispersion curves. Validating these approaches in both controlled laboratory experiments and real-world bridge settings, particularly under known structural modifications or damage conditions, will be crucial for assessing their reliability. A systematic study of how different structural changes influence Lamb wave characteristics will further refine their application for structural health monitoring.

- Uncertainties related to fiber-optic cable coupling, conduit materials, and installation conditions may impact measurement accuracy. Future studies should quantify these factors, assess their effects on long-term monitoring stability under varying environmental and operational conditions, and implement corrections based on analysis of long-term field data recordings.

- This study focuses on box girder bridges, but future work should explore other bridge types and structural forms, such as truss, arch, and cable-stayed bridges. Investigating how different structural configurations influence wave propagation will help generalize our approach to a wider range of bridge infrastructure.

- Establishing damage-sensitive metrics based on Lamb wave measure-

ments will be essential for integrating this approach into practical bridge health monitoring systems. By correlating observed wave propagation changes with structural deterioration, we can develop early warning indicators to support proactive maintenance and risk mitigation efforts.

8. Conclusions

This study demonstrates the feasibility of using DAS to measure wavefields of low-frequency (1-70 Hz) flexural-mode Lamb waves in box girder bridges. By leveraging pre-existing fiber-optic infrastructure, we establish a dense sensing network capable of capturing wave propagation in operational bridges without requiring additional sensor deployment. Our method constructs virtual shot gathers from ambient traffic vibrations, avoiding disruptions to regular traffic. Additionally, we introduce a simplified yet effective modeling framework that approximates the box girder as an elastic isotropic plate, offering a foundation for characterizing low-frequency Lamb waves. Our approach was successfully validated on two box girder bridges, where the measured dispersion curves closely aligned with theoretical modeling results. These findings highlight the potential of low-frequency Lamb wave measurements using DAS as a novel, non-intrusive technique for continuous bridge health monitoring.

9. Acknowledgements

LUNA-Optasense contributed to the recording of DAS data in San Jose by loaning the instrument and providing field support. In particular, Andres Chavarria facilitated the instrument loaning, and Victor Yartsev helped in the field operations. We also thank Dubai Future Foundation, UnipolTech, Consiglio per la Ricerca in Agricoltura e l'Analisi dell'Economia Agraria, Volkswagen Group America, FAE Technology, Samoo Architects & Engineers, Shell, GoAigua, ENEL Foundation, Kyoto University, Weizmann Institute of Science, Universidad Autónoma de Occidente, Instituto Politecnico Nacional, Imperial College London, Universitá di Pisa, KTH Royal Institute of Technology, AMS Institute and all the members of the MIT Senseable City Lab Consortium for supporting this research. All the members of the MIT Senseable City Lab Consortium do not receive any direct financial or economic advantage from the publication of this study and had no role in study design, data collection and analysis, decision to publish or preparation of the manuscript. We thank Robert Clapp, Siyuan Yuan, Thomas Cullison, and Seunghoo Kim from Stanford University for helping with the data collection, as well as the City of San Jose – particularly Darren Thai and Ho Nguyen – for crucial help with the experiment.

References

[1] Guang-Dong Zhou and Ting-Hua Yi. Recent developments on wireless sensor networks technology for bridge health monitoring. *Mathematical*

Problems in Engineering, 2013(1):947867, 2013.

[2] Zhihang Deng, Minshui Huang, Neng Wan, and Jianwei Zhang. The current development of structural health monitoring for bridges: A review. *Buildings*, 13(6), 2023.

[3] F. Magalhães, A. Cunha, and E. Caetano. Vibration based structural health monitoring of an arch bridge: From automated oma to damage detection. *Mechanical Systems and Signal Processing*, 28:212–228, 2012. Interdisciplinary and Integration Aspects in Structural Health Monitoring.

[4] Juan Pablo Amezquita-Sanchez and Hojjat Adeli. Signal processing techniques for vibration-based health monitoring of smart structures. *Archives of Computational Methods in Engineering*, 23:1–15, 2016.

[5] X. W. Ye, C. Z. Dong, and T. Liu. A review of machine vision-based structural health monitoring: Methodologies and applications. *Journal of Sensors*, 2016(1):7103039, 2016.

[6] Jingxiao Liu, Yujie Wei, and Bingqing Chen. A hierarchical semantic segmentation framework for computer vision-based bridge damage detection. *Smart Structures and Systems*, 31(4):325–334, 2023.

[7] Jingxiao Liu, Siheng Chen, Mario Bergés, Jacobo Bielak, James H. Garrett, Jelena Kovačević, and Hae Young Noh. Diagnosis algorithms for

indirect structural health monitoring of a bridge model via dimensionality reduction. *Mechanical Systems and Signal Processing*, 136:106454, 2020.

[8] Jingxiao Liu, Susu Xu, Mario Bergés, and Hae Young Noh. Hiermud: Hierarchical multi-task unsupervised domain adaptation between bridges for drive-by damage diagnosis. *Structural Health Monitoring*, 22(3):1941–1968, 2023.

[9] Jingxiao Liu. *Accurate and Scalable Bridge Health Monitoring Using Drive-By Vehicle Vibrations*. Stanford University, 2023.

[10] Jingxiao Liu, Haipeng Li, Hae Young Noh, Paolo Santi, Biondo Biondi, and Carlo Ratti. Urban sensing using existing fiber-optic networks. *arXiv preprint arXiv:2409.05820*, 2024.

[11] Nathaniel J. Lindsey and Eileen R. Martin. Fiber-optic seismology. *Annual Review of Earth and Planetary Sciences*, 49(Volume 49, 2021):309–336, 2021.

[12] Zhongwen Zhan. Distributed acoustic sensing turns fiber-optic cables into sensitive seismic antennas. *Seismological Research Letters*, 91(1):1–15, 12 2019.

[13] Siyuan Yuan, Jingxiao Liu, Hae Young Noh, Robert Clapp, and Biondo Biondi. Using vehicle-induced das signals for near-surface characterization with high spatiotemporal resolution. *Journal of Geophysical*

Research: Solid Earth, 129(4):e2023JB028033, 2024. e2023JB028033 2023JB028033.

[14] Jingxiao Liu, Haipeng Li, Siyuan Yuan, Hae Young Noh, and Biondo Biondi. Characterizing vehicle-induced distributed acoustic sensing signals for accurate urban near-surface imaging. *arXiv preprint arXiv:2408.14320*, 2024.

[15] Haipeng Li, Jingxiao Liu, Shujuan Mao, Siyuan Yuan, Robert G Clapp, and Biondo L Biondi. Daily groundwater monitoring using vehicle-das elastic full-waveform inversion. *arXiv preprint arXiv:2501.10618*, 2025.

[16] Jingxiao Liu, Siyuan Yuan, Yiwen Dong, Biondo Biondi, and Hae Young Noh. Telecomtm: A fine-grained and ubiquitous traffic monitoring system using pre-existing telecommunication fiber-optic cables as sensors. *Proc. ACM Interact. Mob. Wearable Ubiquitous Technol.*, 7(2), June 2023.

[17] *Urban system monitoring using combined vehicle onboard sensing and roadside distributed acoustic sensing*, volume Day 1 Sun, September 26, 2021 of *SEG International Exposition and Annual Meeting*, 09 2021.

[18] Jingxiao Liu, Siyuan Yuan, Bin Luo, Biondo Biondi, and Hae Young Noh. Turning telecommunication fiber-optic cables into distributed acoustic sensors for vibration-based bridge health monitoring. *Structural Control and Health Monitoring*, 2023(1):3902306, 2023.

[19] Julie Rodet, Benoit Tauzin, Mohammad Amin Panah, Philippe Guéguen, Destin Nziengui Bâ, Olivier Coutant, and Stéphane Brûlé. Urban dark fiber distributed acoustic sensing for bridge monitoring. *Structural Health Monitoring*, 24(1):636–653, 2025.

[20] A. K. Maji, D. Satpathi, and T. Kratochvil. Acoustic emission source location using lamb wave modes. *Journal of Engineering Mechanics*, 123(2):154–161, 1997.

[21] I. J. Oppenheim, D. W. Greve, and N. L. Tyson. Lamb wave behavior in bridge girder geometries. In Masayoshi Tomizuka, Chung-Bang Yun, and Victor Giurgiutiu, editors, *Smart Structures and Materials 2006: Sensors and Smart Structures Technologies for Civil, Mechanical, and Aerospace Systems*, volume 6174, page 61742E. International Society for Optics and Photonics, SPIE, 2006.

[22] Jiao Jingpin, Meng Xiangji, He Cunfu, and Wu Bin. Nonlinear lamb wave-mixing technique for micro-crack detection in plates. *NDT & E International*, 85:63–71, 2017.

[23] Younho Cho, D.D. Hongerholt, and J.L. Rose. Lamb wave scattering analysis for reflector characterization. *IEEE Transactions on Ultrasonics, Ferroelectrics, and Frequency Control*, 44(1):44–52, 1997.

[24] Horace Lamb. On waves in an elastic plate. *Proceedings of the Royal*

Society of London. Series A, Containing Papers of a Mathematical and Physical Character, 93(648):114–128, 1917.

[25] Zhongqing Su and Lin Ye. *Identification of damage using Lamb waves: from fundamentals to applications*, volume 48. Springer Science & Business Media, 2009.

[26] J. D. Achenbach. Lamb waves as thickness vibrations superimposed on a membrane carrier wave. *The Journal of the Acoustical Society of America*, 103(5):2283–2286, 05 1998.

[27] Nils Ryden, Choon B. Park, Peter Ulriksen, and Richard D. Miller. Lamb wave analysis for non-destructive testing of concrete plate structures. 2003.

[28] D C Worlton. Ultrasonic testing with lamb waves. Technical report, General Electric Co., Hanford Atomic Products Operation, Richland, Wash., 09 1956.

[29] B.S. Ben, B.A. Ben, K.A. Vikram, and S.H. Yang. Damage identification in composite materials using ultrasonic based lamb wave method. *Measurement*, 46(2):904–912, 2013.

[30] Qingfei Gao, Zonglin Wang, Hongyu Jia, Chenguang Liu, Jun Li, Binqiang Guo, and Junfei Zhong. Dynamic responses of continuous girder bridges with uniform cross-section under moving vehicular loads. *Mathematical Problems in Engineering*, 2015(1):951502, 2015.

[31] Young Hak Lee and Taekeun Oh. The simple lamb wave analysis to characterize concrete wide beams by the practical MASW test. *Materials*, 9(6), 2016.

[32] Stephen A Hambric. Structural acoustics tutorial—part 1: vibrations in structures. *Acoustics Today*, 2(4):21–33, 2006.

[33] Nori Nakata, Lucia Gualtieri, and Andreas Fichtner. *Seismic ambient noise*. Cambridge University Press, 2019.

[34] Kees Wapenaar, Deyan Draganov, Roel Snieder, Xander Campman, and Arie Verdel. Chapter 15 seismic interferometry: Tutorial on seismic interferometry: Part 1 — basic principles and applications. In *Geophysics Today: A Survey of the Field as the Journal Celebrates its 75th Anniversary*. Society of Exploration Geophysicists, 01 2010.

[35] Kees Wapenaar. Retrieving the elastodynamic green's function of an arbitrary inhomogeneous medium by cross correlation. *Phys. Rev. Lett.*, 93:254301, Dec 2004.

[36] Optasense, a Luna company. QuantX DAS interrogator: Optasense, 2022.

[37] G. D. Bensen, M. H. Ritzwoller, M. P. Barmin, A. L. Levshin, F. Lin, M. P. Moschetti, N. M. Shapiro, and Y. Yang. Processing seismic ambient noise data to obtain reliable broad-band surface wave dispersion

measurements. *Geophysical Journal International*, 169(3):1239–1260, 06 2007.

[38] Choon Byong Park, Richard D. Miller, and Jianghai Xia. *Imaging dispersion curves of surface waves on multi-channel record*, pages 1377–1380. 2005.